Molecular dynamics simulations on mechanical behaviors of sintered nanocopper in power electronics packaging

Luo, Runding; Hu, Dong; Qian, Cheng; Liu, Xu; Fan, Xuejun; Zhang, Guoqi; Fan, Jiajie

DOI
10.1016/j.microrel.2023.115284

Publication date
2024

Document Version
Final published version

Published in
Microelectronics Reliability

Microelectronics Reliability 152 (2024) 115284

Contents lists available at ScienceDirect

Microelectronics Reliability

journal homepage: www.elsevier.com/locate/microrel

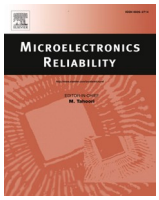

Molecular dynamics simulations on mechanical behaviors of sintered nanocopper in power electronics packaging

Runding Luo [a], Dong Hu [b], Cheng Qian [a], Xu Liu [a], Xuejun Fan [d], Guoqi Zhang [a,b], Jiajie Fan [a,b,c,*]

[a] Institute of Future Lighting, Academy for Engineering & Technology, Shanghai Engineering Technology Research Center for SiC Power Device, Fudan University, Shanghai 200433, China
[b] EEMCS Faculty, Delft University of Technology, Delft, the Netherlands
[c] Research Institute of Fudan University in Ningbo, Ningbo 315336, China
[d] Department of Mechanical Engineering, Lamar University, Beaumont, TX, USA

ARTICLE INFO

Keywords:
Nano-Cu sintering
Molecular dynamics (MD) simulation
Nanoflake
Shear simulation
Tensile simulation

ABSTRACT

Nano-metal materials have received considerable attention because of their promising performance in wide bandgap semiconductor packaging. In this study, molecular dynamics (MD) simulation was performed to simulate the nano-Cu sintering mechanism and the subsequent mechanical behaviors. Hybrid sintering, comprising nanosphere (NS) and nanoflake (NF), was performed at temperatures from 500 to 650 K. Furthermore, shear and tensile simulations were conducted with constant strain rates on the sintered structure at multiple temperatures. Subsequently, the extracted mechanical properties were correlated with the sintering behavior. The results revealed that the mechanical properties of the nano-Cu sintered structure could be improved by tuning material composition and increasing the sintering temperature. We established a relationship between the sintered microstructure and mechanical response. The shear modulus and shear strength of the sintered structure with NF particles increased to 41.20 and 3.51 GPa respectively. Furthermore, the elastic modulus increased to 55.60, and the tensile strength increased to 4.88 GPa. This result provides insights into the preparation phase of nano-Cu paste for sintering technology.

1. Introduction

Wide bandgap (WBG) semiconductors such as SiC and GaN can be applied in strategic industries, such as renewable energy technology, high-speed railways, and intelligent vehicle. Improving the power density, higher operating temperature, functionalization, and miniaturization of WBG has attracted considerable research attention [1,2]. To ensure the reliability and functionality of the WBG semiconductor package, the development of a low process temperature joining technology with superior stability at high temperature is necessary.

The sintering of nano-metal materials provides numerous benefits, such as improved electrical interconnection, mechanical support, and heat dissipation channels for WBG power module packaging. Furthermore, sintering leverages the nanosize effects to achieve "low-temperature packaging, high-temperature operation" [3]. Compared with nano-Ag, the nano-Cu paste has a higher melting point, lower material cost, excellent thermal conductivity, and matching thermal coefficient of expansion. Therefore, this method can become the interconnection material for the next generation of high-power electronic packaging [4–6].

The addition of NF can effectively reduce the porosity of the sintered structure by promoting the sintering rate and sintering neck growth [7–11]. Unlike the sphere-shape nanoparticle, the NF particles continuously deform during the sintering process [12]. Dislocations caused by deformation generate stress inside the particle, and stress release promotes the sintering process.

However, the relationship between particle geometry, sintering condition, and microstructure evolution during Cu sintering has been rarely reported. Li [13] simulated and analyzed the Ag sintering mechanism with the addition of Ag NF. Cheng [14] studied the sintering of a multi-particle Cu NP system at multiple temperatures and pressures. In addition, numerous simulations have been conducted to connect the sintered structure with mechanical properties. Hu [15] studied the sintering dynamics of pressure-assisted Cu NPs and subsequently simulated

* Corresponding author at: Institute of Future Lighting, Academy for Engineering & Technology, Shanghai Engineering Technology Research Center for SiC Power Device, Fudan University, Shanghai 200433, China.
E-mail address: jiajie_fan@fudan.edu.cn (J. Fan).

https://doi.org/10.1016/j.microrel.2023.115284
Received 18 July 2023; Received in revised form 23 October 2023; Accepted 19 November 2023
Available online 30 November 2023

tensile strength through a uniaxial tension at a constant strain rate.

This study used the MD method to simulate the sintering of two Cu nanoparticles and investigated their mechanical behavior. Furthermore, the sintering kinetics and microstructure evolution of multi-models comprising equal/non-equal-dimension Cu nanospheres and nanoflakes were used to determine the effect of geometry on the sintering process. Simulations were conducted at various sintering temperatures (from 500 to 650 K) to identify the dominant sintering mechanism in each model. In addition, the mechanical behavior was analyzed using constant rate shear simulation. This study integrated the process temperature, sintered structure, and mechanical response and demonstrated the potential of the methodology for determining material and process conditions for future nano-Cu sintering technology.

2. Methods and modeling

2.1. Atomistic modeling

In this study, the classical embedded atom method (EAM) potential developed by Adam [16] was used to describe the interaction between Cu atoms. This potential has been proved to accurately describe Cu inter-atomic properties [17,18]. The total energy of the system based on this force field is as follows:

$$E_i = F_\alpha\left(\sum_{j\neq i}\rho_\beta(r_{ij})\right)+\frac{1}{2}\sum_{j\neq i}\varphi_{\alpha\beta}(r_{ij}) \quad (1)$$

Here, α and β are the element types of atoms i and j. Furthermore, F is the embedded energy and φ is the pairwise interactions, which are a function of the atom types α and β and the atomic spacing r_{ij}.

Fig. 1 displays two types of sintering structures constructed in sintering simulation, namely the nanosphere (NS)–NS model and the NS–nanoflake (NF) model to investigate the effect of various particle size ratios (1:1–1:3) and the addition of NF on sintering. The diameter of NS was set to 5, 10, and 15 nm. The length of NF particles was set to 5 and 10 nm, the length-to-thickness ratio was 5:2. To eliminate the influence of model orientation, all components were initially set at the ⟨100⟩ orientation. Furthermore, 3.6 Å was considered the initial spacing between pair of particles, which is the Cu lattice constant value.

In this study, molecular dynamic simulation was performed using the large-scale atomic/molecular massively parallel simulator (LAMMPS) [19]. The simulation results were visualized using the open visualization tool (OVITO) [20].

2.2. Simulation flow

All simulations were performed in a three-dimensional simulation box with periodic boundaries with a time step of 1 fs. The NVT ensemble was adopted for sintering simulation. Fig. 2 displays the simulation profile. Prior to system assembly, the NS and NF were relaxed at the sintering temperature within 50 ps to obtain equilibrium.

Before the sintering simulation, the system energy was at first minimized through the steepest descent algorithm. Next, the model was simulated for 500 ps at sintering temperature T_{sinter} to ensure a post-sintering equilibrium status. A relaxation step follows sintering till the model comes back to shear temperature T_{shear}. Subsequently, shear simulation was performed within 200 ps. Tensile simulation followed a similar procedure as shear simulation. Before sintering simulation, the system energy was minimized, and after the sintering process, a relaxation process was performed. When the model returned to the tensile temperature, tensile simulation was performed within 200 ps.

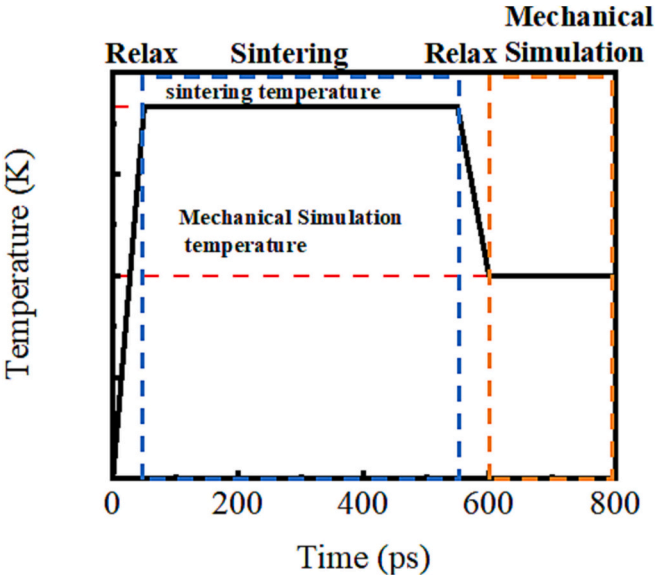

Fig. 2. Nano-Cu mechanical simulation process.

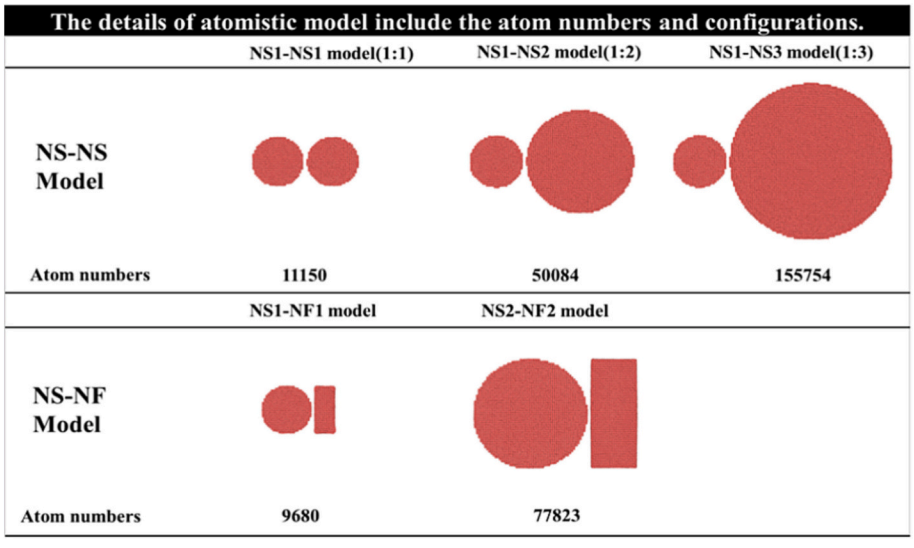

Fig. 1. Atomistic models in sintering simulation.

2.3. Sintering process simulation

In sintering simulations, considering the sintering temperature in reported studies, sintering simulation temperatures of 500, 550, 600, and 650 K were considered. The sintering process was evaluated by the total dislocation length, lattice transformation, and geometry evolution. In this study, dislocation analysis and common neighbor analysis were used to characterize sintered microstructures. Furthermore, the ratio of the neck size (x) to the dimension of the particles (W) is defined as x/W, as displayed in Fig. 3. To obtain the size of the neck, a dynamically distributed block with a thickness of 3.5 Å was defined in the neck region, which contained less than three layers of nano-Cu atoms. Mean Square Displacement (MSD) was used to evaluate the sintering mechanism of the model and determine the rate of diffusion. The formula for calculating MSD is as follows:

$$\mathrm{MSD} = \frac{1}{N}\sum_{i=1}^{N}\left[r_i(t) - r_i(0)\right]^2 \tag{2}$$

where N is the number of atoms, r_i(t) and r_i(0) are the positions of atom i at time t and time 0, respectively.

2.4. Mechanical simulation

To evaluate the adhesive strength of each sintered structure, shear simulation and sintering simulation with variable temperatures were performed on the sintered model with a constant strain rate. In shear simulation, shear temperatures of 300, 450, and 600 K were used to simulate the mechanical response. Two baseplates were added to implement shear simulation, as displayed in Fig. 4. The upper plate was used to apply a constant speed of 0.2 Å/fs along the ⟨100⟩ direction. In tensile simulation, the mechanical responses at various tensile temperatures, namely 300, 450, and 600 K, were simulated. The substrate was used to apply tensile strain rates of 0.01 and 0.001 ps^{-1} along the ⟨010⟩ direction. By contrast, the lower plate was applied to fix the position of the model. The length of the upper and lower substrates was two times the diameter of the larger component and the thickness was 1 nm.

The stress–strain curve of the sintered region was obtained in shear simulation. The monoatomic stress tensor of the sintered Cu atoms can be obtained as follows:

$$S_{ab} = -mv_a v_b - W_{ab} \tag{3}$$

where a and b have values x, y, and z to generate the components of the tensor. The first term is a kinetic energy contribution and W_{ab} is the virial contribution.

To eliminate the influence of the volume term, the component of monatomic stress is summed and divided by the volume of the sintered region as follows:

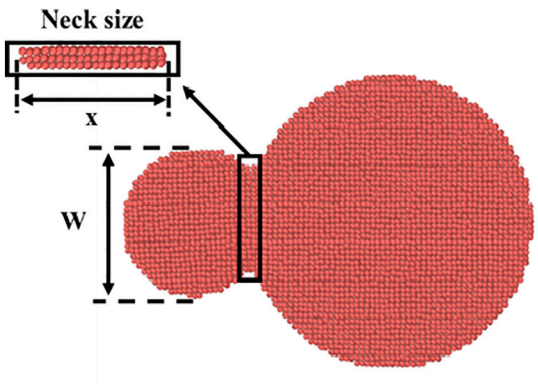

Fig. 3. NS–NS model and geometric parameters for sintering simulation.

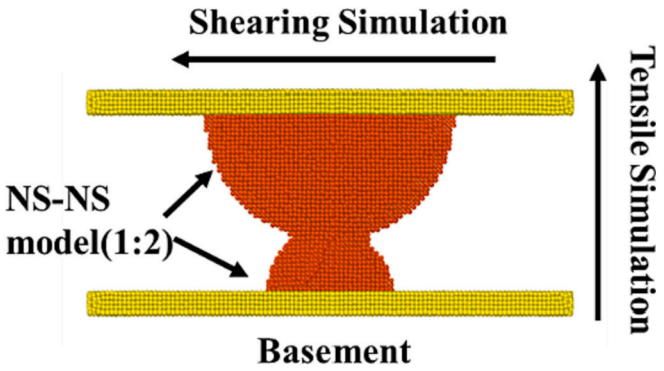

Fig. 4. NS–NS model and geometric parameters for mechanical simulation.

$$\sigma = \frac{1}{N}\sum_{i=1}^{N}\left(\frac{p_i \div v_i}{-10000}\right) \tag{4}$$

where σ is the average stress value of the sintered region, N is the number of atoms, p is the calculated value of the i_{th} atom, and v is the volume term of the i_{th} atom.

Shear fracture in an FCC metal occurs along the close-packed plane at 45° to the shear direction. Thus, the XZ stress tensor component was adopted to derive the stress.

3. Simulation results and discussion

3.1. Sintering process simulations

3.1.1. Effect of geometry on sintering

Figs. 5(a) and (b) and 6(a) and (b) detail the evolution in total dislocation length and Hexagonal Close Packing (HCP) ratio during the 500 K sintering of the NS–NF and the NS–NS models. The details in the blue frames are enlarged and placed aside. The sintering process was categorized into several stages according to the dislocation behavior, as displayed in Figs. 5(c) and 6(c).

In the first stages, the two components approach each other and result in no change in either the dislocation length or the HCP ratio. Next, the dislocation length of the NF–NS model started to rapidly increase at state ⟨2⟩ (6 ps). However, it occurs in an NS–NS model at 26 ps. Fig. 5(c) reveals a small necking region formed at this step with minor dislocations and HCP crystal structures generated in the neck region. Next, the neck grows rapidly, and the dislocations increase continuously, producing a small number of HCP atoms in state ⟨3⟩, and the dislocation reached its maximum in state ⟨4⟩. However, far more dislocations were generated in the NS–NF model than in the NS–NS model. This phenomenon could be attributed to the NF bent toward the NS during sintering, and generation of more dislocations to accommodate the deformation.

To investigate the influencing factors of geometries and the size ratio, the evolution of x/W and MSD on the NS–NS and NS–NF models is plotted in Fig. 7. The nonequal diameter NS–NS models obtained a larger necking region than the equal diameter NS–NS model. However, tuning the particle size had a limited effect on the improvement of the sintered neck length from the results of NS1–NS2 and NS1–NS3 models. Furthermore, the x/W of the NS–NF model outperformed NS–NS models with the same dimension. The x/W of the NS–NF model was 1.2 times higher than that of the NS–NS model. This result proved that the participation of NF particles considerably improved the sintering neck size.

The sintering mechanism of various models was investigated through MSD, as displayed in Fig. 7(b). The slope of the MSD curve was proportional to the diffusion rate, and the rapid increase in MSD in the initial stage contributed to plastic deformation. The presence of the NF

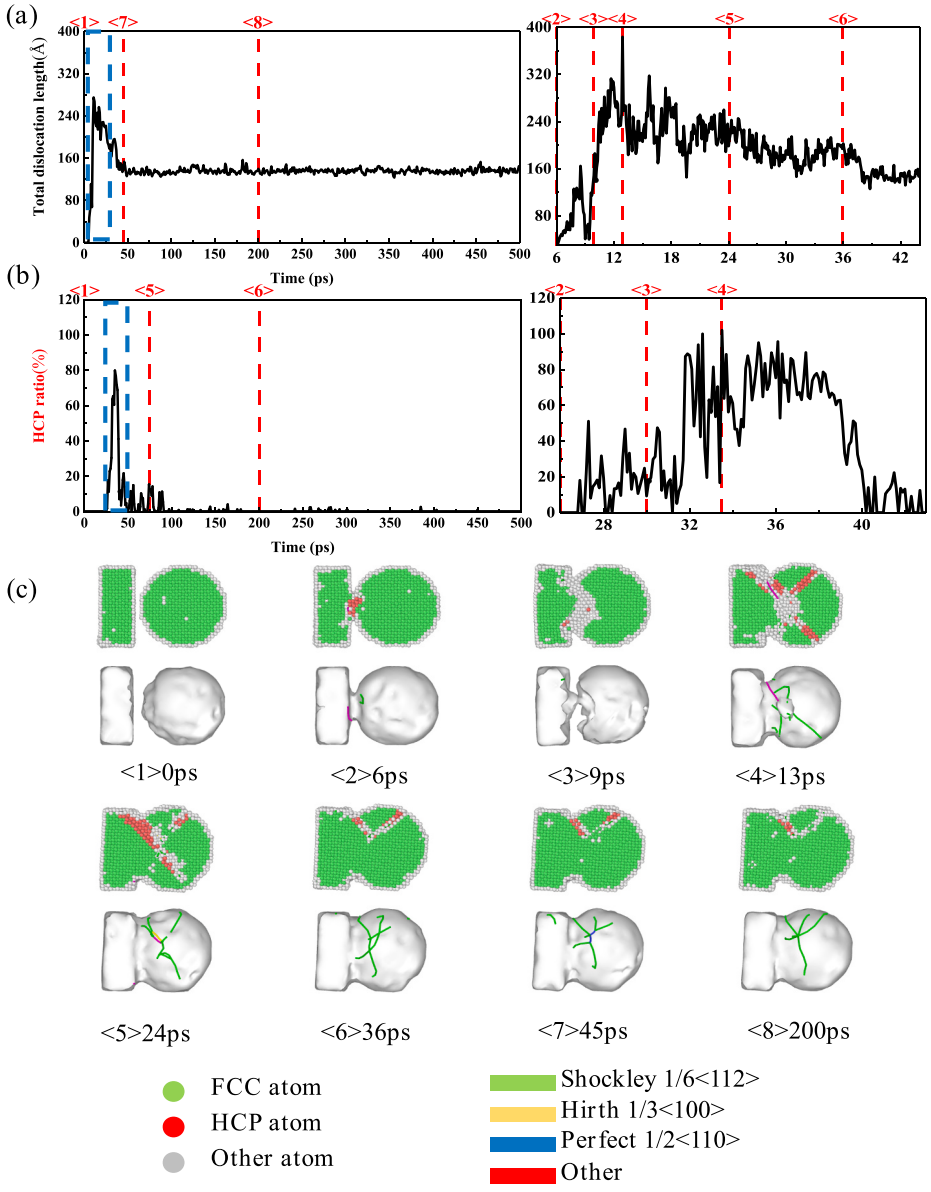

Fig. 5. Evolution of the (a) total dislocation length and (b) HCP ratio during sintering; (c) Snapshots of NS–NF during sintering: Lattice structures, HCP lattice structure, and dislocations.

not only accelerated the diffusion rate of atoms but also rendered the plastic flow between Cu NPs to be more intense, which is caused by the neck size of the NF–NS model being larger than that of the NS–NS model.

Therefore, we have the following: (1) the nonequal diameter NS–NS model had a larger sintering neck size than the equal diameter NS–NS model; (2) the NS–NF model can promote the sintering performance compared with the equal diameter NS–NS models; (3) the presence of NF enhanced plastic deformation during sintering by promoting atomic diffusion on the surface and volume of the particles as well as generating more defects. The stress release caused by these defects promoted the sintering of nanoparticles.

3.1.2. *Effect of temperature on sintering*

Various temperatures were applied to the NS1–NS1 and NS1–NF1 models. Fig. 8 plots the x/W curve as a function of the sintering time at various sintering temperatures. Compared with the NS–NF model, the sintered neck growth of the NS–NS model was highly sensitive to the sintering temperature. Higher sintering temperature resulted in a larger x/W ratio. By contrast, the neck size of the NS–NF model remained stable according to the increase in temperature. The difference in the temperature dependence implies that the sintering process of the NS–NF model was less dominated by surface diffusion, in which the sintering temperature played an essential role.

The results can be verified by the MSD of NS–NF and NS–NS models at various temperatures in Fig. 9. In the NS–NS model, improving the sintering temperature resulted in considerable promotion in the MSD. Furthermore, the slope in the rapid increase stage also indicated a higher diffusion rate at higher temperatures. Sintering in the NS–NS model was attributed to surface diffusion. By contrast, the MSD rapid stage in the NS–NF model ended at 10 ps, but the x/W ratio still increased, which indirectly proved that mass migration was contributed by the plastic flow instead of the surface diffusion at this time. The slope of the NS–NF model was larger than that of the NS–NS model.

3.2. *Shear process simulations*

3.2.1. *Microstructure analysis of shear simulations*

Shear simulation was performed on the post-sintered atomistic

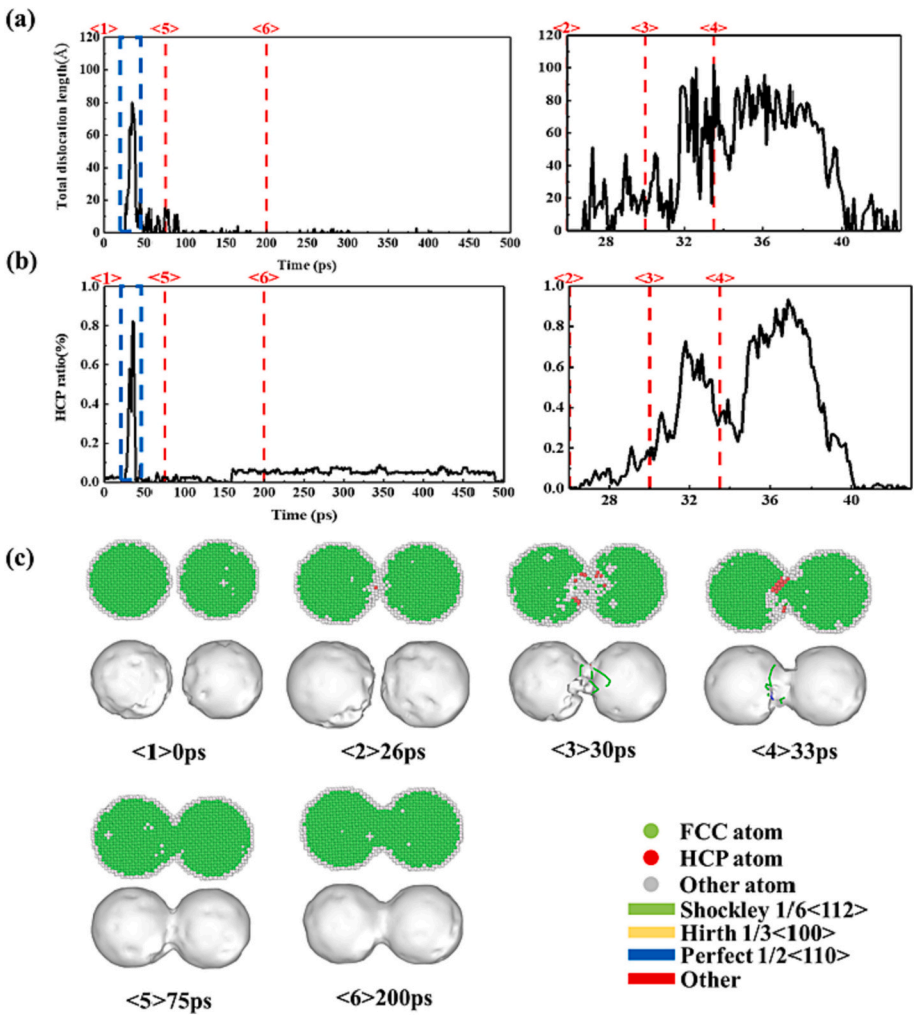

Fig. 6. Evolution of the (a) total dislocation length and (b) HCP ratio during sintering; (c) Snapshots of NS–NS during sintering: Lattice structures, HCP lattice structure, and dislocations.

model. Considering the practical experimental condition, shear tests were simulated at 300, 450 and 600 K. Fig. 10 displays the stress–strain curves and dislocation length evolution of the NS1–NS2 model sintered at 500 K. Moreover, the shear process was divided into six key time points according to the stress evolution. Fig. 11 displays the model snapshots at each time point. The results revealed that the sintered NS1–NS2 model can withstand shear stress close to 1.5 GPa. A small stress concentration was observed in the neck region before shear, which was attributed to the residual Stacking Fault (SF) from sintering. In shear simulation, the stress increased rapidly with the increase in strain at the beginning at state ⟨1⟩, and the model was in the elastic stage. Then, stress–strain curve followed Hooke's law, the curve of the elastic stage was fitted, and its slope can be the shear modulus of the sintered model. Subsequently, the sintered model entered the yield phase, and the stress fluctuated up and down with the increase in strain, as in states ⟨2⟩-⟨4⟩. At this stage, the dislocation length first decreased and subsequently increased. The dislocation direction in the model changed from northwest to northeast because during the shear process, dislocations generated during sintering were constantly disassembled, and new dislocations formed under the action of shear stress. Finally, the sintered structure entered the viscoplastic deformation stage, and the stress decreased continuously with the increase in strain until it tended to 0. The maximum stress in the critical fracture phase of the nano-Cu sintered structure was the shear strength.

From states ⟨2⟩ to ⟨6⟩, the neck of Cu NPs shrank continuously with the movement of the upper basement, which resulted in a serrated evolution of stress. This phenomenon could be attributed to the dislocation nucleation, propagation, and eventual decomposition to achieve plastic deformation. This dislocation behavior continuously occurs under the objected external force, which results in structural instability.

3.2.2. *Effects of process parameters on the mechanical properties*

Fig. 12(a) and (b) displays the stress–strain curves of NS–NS and NS–NF models at various shear temperatures. After entering the yield stage, the curves fluctuated considerably during the plastic deformation process. In this stage, the model structure was more complex. The structure changed with the increase in dislocation activity, and the sintering neck area changed considerably. The shear strength and shear modulus decreased with the increase in the shear temperature. The shear strength of the NS1–NS1 model was 2.47 GPa at 600 K, which was lower than that of the value extracted at the 300 K shear temperature. The shear strength improved considerably after adding the NF particles. At the shear temperature of 600 K, the shear strength increased by 25 %, reaching 3.04 GPa.

Fig. 13 reveals that increasing the sintering temperature of the NS1–NS1 model to 650 K increased the shear strength and shear modulus. The larger the neck size, the better the shear modulus and shear strength of the sintered structure. Fig. 14 displays the stress–strain curves of various initial models. The NS1–NF1 model achieved excellent mechanical properties. When the size of sintered particles increased, the

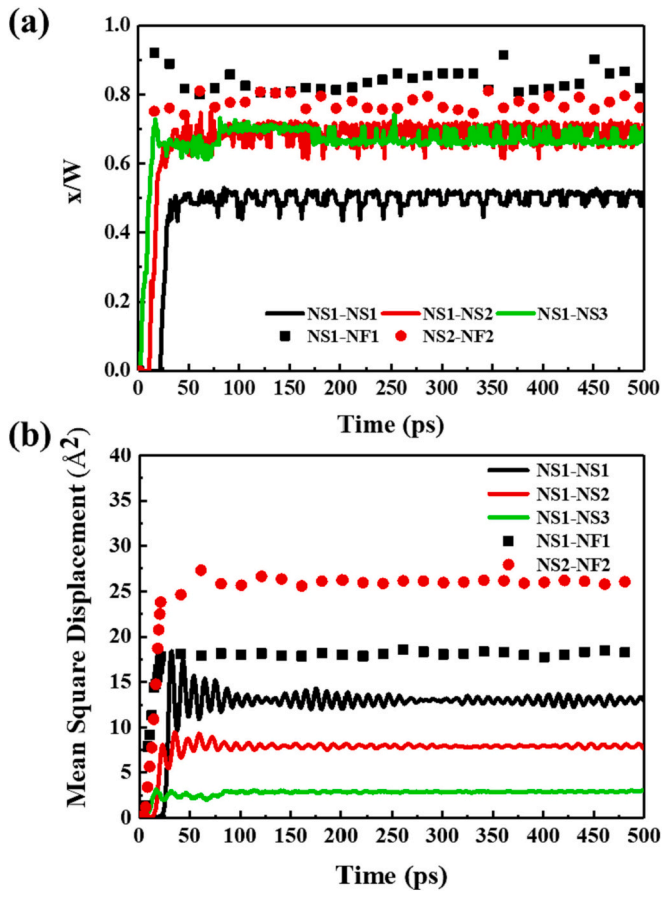

Fig. 7. (a) The x/W at 500 K sintering temperature for various models; (b) MSD at the 500 K sintering temperature for different models.

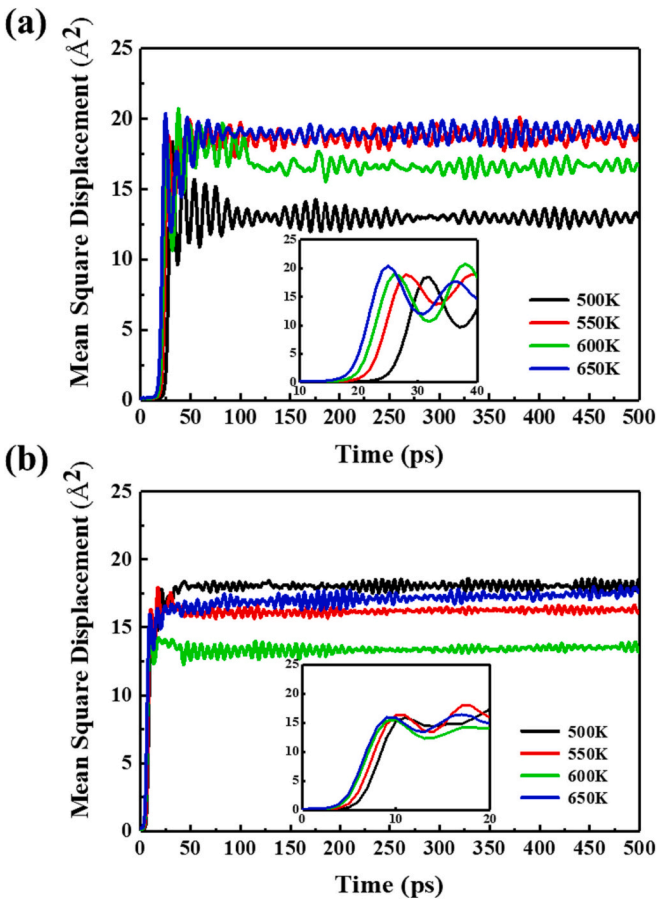

Fig. 9. (a) MSD of NS1–NS1 model at various temperatures; (b) MSD of NS1–NF1 model at various temperatures.

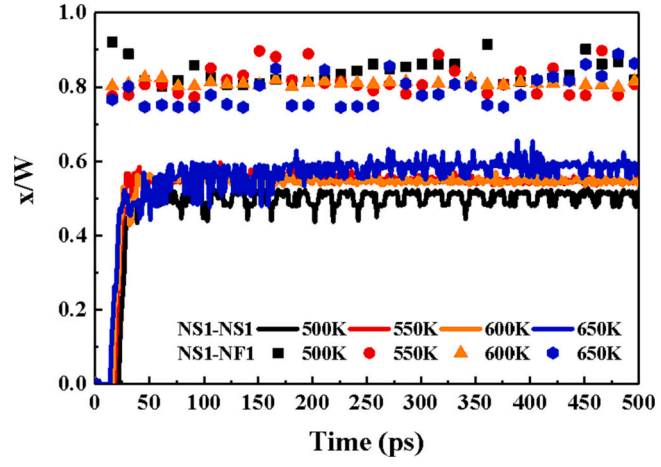

Fig. 8. x/W for NS–NS and NS–NF models at various sintering temperatures.

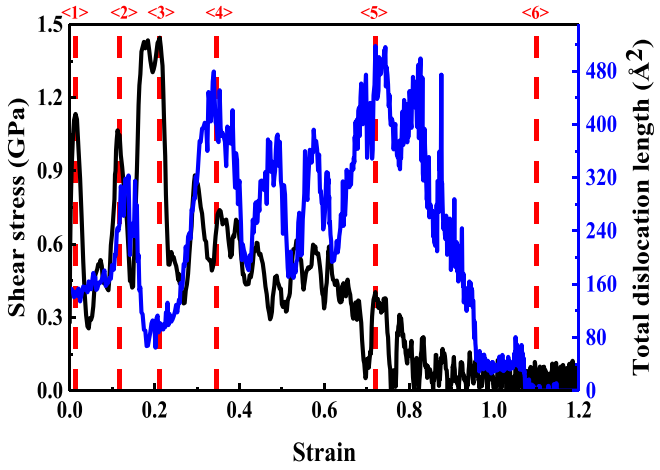

Fig. 10. Shear stress and the total dislocation length in NS1–NS2 shear simulation.

shear strength of the NS2–NF2 model decreased compared with the NS1–NF1 model. The diffusion and plastic mechanisms may not be sufficient to promote the sintering of large-size particles at 500 K, and incomplete sintering resulted in a decrease in mechanical properties. The shear stress variation of nonequal dimension NS–NS model was considerable. This phenomenon could be attributed to the model size of the stress derived from a small particle being affected more by dislocation activity.

3.3. *Tensile process simulations*

3.3.1. *Microstructure analysis of tensile simulations*

Before tensile simulation, the model was relaxed to eliminate defects that occurred during sintering. Fig. 15 displays the Shear stress curves and dislocation length evolution of the NS1–NS2 model sintered at 500 K. Uniaxial constant strain rate tensile simulation was performed on the sintered model, as displayed in state ⟨1⟩ in Fig. 16. Prior to the onset of yield, the nano-Cu sinter underwent elastic deformation, and the tensile

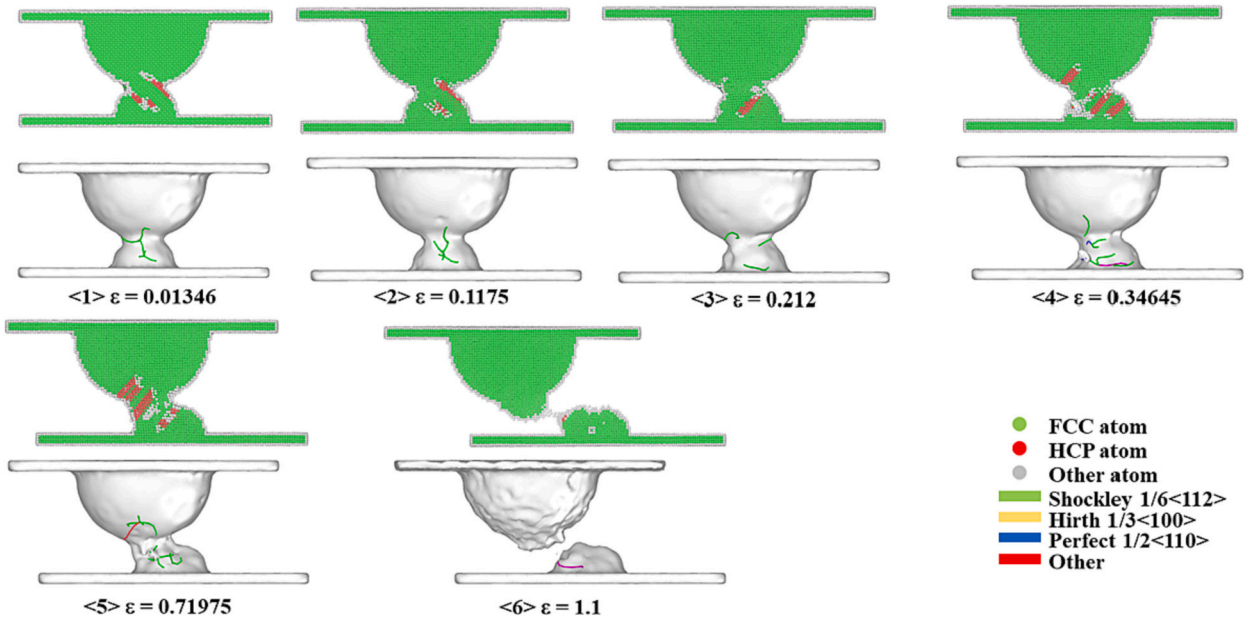

Fig. 11. Snapshots of NS1–NS2 model during sintering: Lattice structures, HCP lattice structure, and dislocations.

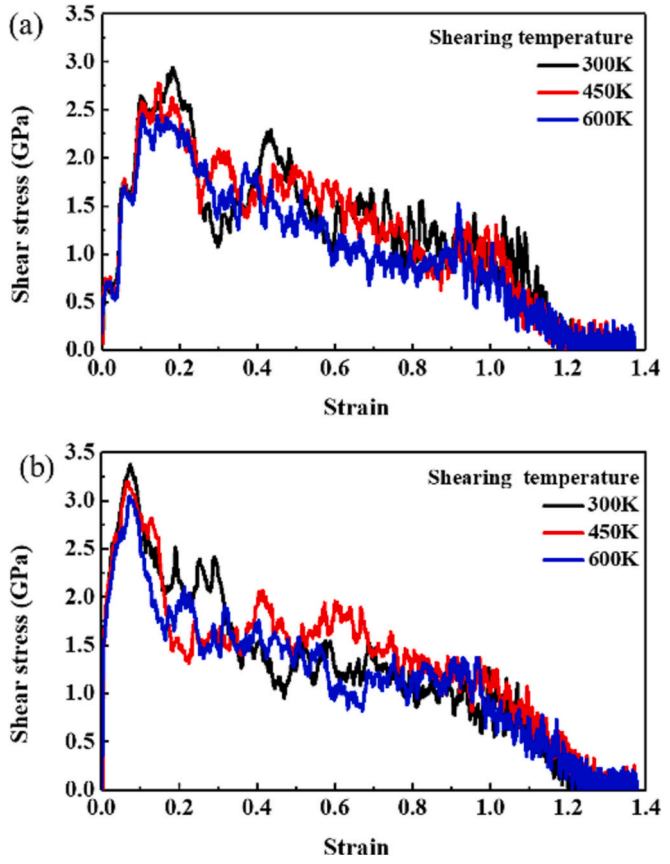

Fig. 12. (a) Shear stress in NS1–NS1 at various shear temperatures; (b) Shear stress in NS1–NF1 at various shear temperatures.

stress increased almost linearly, reaching 5.23 GPa. During this stage, the deformation followed Hooke's law. When tensile simulation progressed to state ⟨2⟩ at 5 ps, dislocations gradually formed and increased considerably within a short period of time, which resulted in stress release and the model entering the yield stage. At state ⟨3⟩, the total

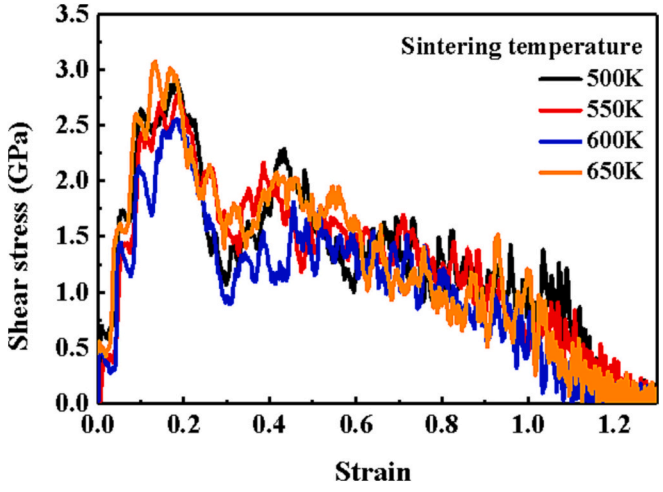

Fig. 13. NS1–NS1 shear simulation of shear stress at various sintering temperatures.

length of dislocations reached its peak value. At this stage, under the action of stress, numerous dislocations were generated in both the upper and lower hemispheres, and these dislocations moved under the applied stress, forming an almost 45° angle misalignment. This phenomenon indicated that the structure had entered the plastic deformation stage, and the sintered neck continuously narrowed as tensile simulation progressed.

At state ⟨4⟩, dislocation entanglement occurred near the neck of the bottom Cu particles. The formation of twin boundaries primarily occurred in the upper hemisphere, accompanied by a partial transformation of the FCC crystal structure into an amorphous structure. Defects in the lower hemisphere moved upward and partially decomposed under the influence of tensile stress. From states ⟨2⟩ to ⟨5⟩, the stress exhibited a sawtooth-like evolution. The current structure was in an unstable state, and the defects induced by the tensile simulation continuously moved and decomposed. When the model reached state ⟨5⟩, the dislocations in the lower hemisphere were mostly decomposed, leaving twin boundaries in the upper hemisphere. The model tended to stabilize. At 60 ps, the stress fluctuated by approximately 0, which

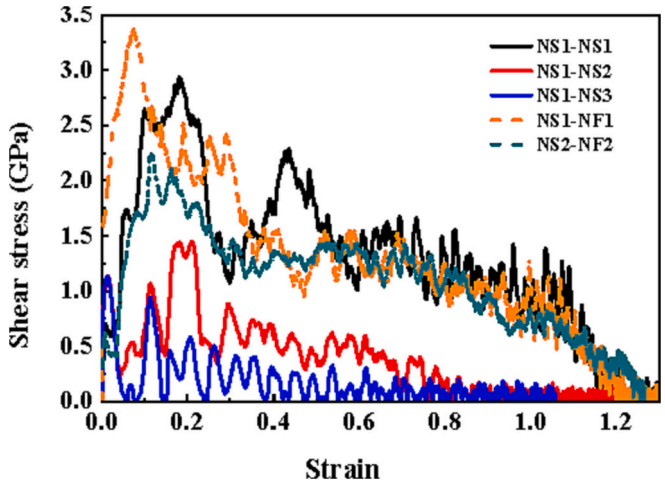

Fig. 14. Shear stress of various sintered structures at a sintering temperature of 500 K.

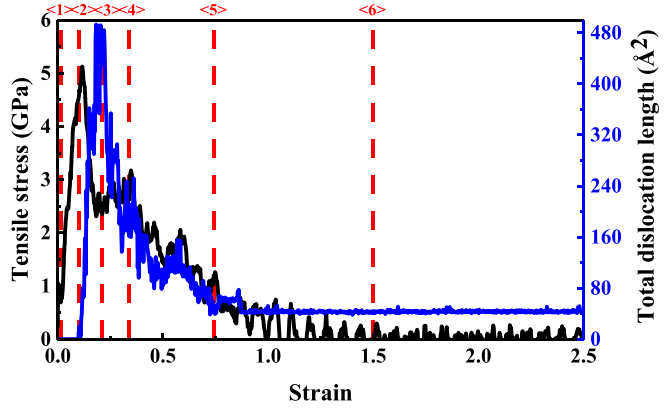

Fig. 15. Shear stress and total dislocation length in NS1–NS2 shear simulation.

indicated the end of tensile simulation.

3.3.2. *Effects of process parameters on mechanical properties*

Fig. 17(a) and (b) displays the stress–strain curves of sintered Cu NPs under various tensile temperatures. The tensile strength increased considerably as the tensile temperature decreased. At 300 K, both sintered structures exhibited a tensile strength >4 GPa. For the flake and spherical models, the tensile strength did not change considerably as the tensile temperature increased from 300 to 450 K. However, when the tensile temperature reached 600 K, both models exhibited a notable decrease in the tensile strength. In contrast to the results in shear simulation, the NS–NS model exhibited a tensile strength of 4.526 GPa at a strain rate of 0.001 ps^{-1} and 300 K, which was higher than the model with added NF particles. The inclusion of flake particles decreases the overall tensile strength of the model. Fig. 18 demonstrates that the tensile rate considerably affects the tensile performance of both models. Decreasing the strain rate of the NS–NS model from a high rate of 0.01 ps^{-1} to a low rate of 0.001 ps^{-1} results in a decrease in the tensile strength from 5.545 to 4.526 GPa, which revealed a reduction of 18.4 %.

Fig. 19 reveals that increasing the sintering temperature of the NS1–NF1 model leads to an increase in both the tensile strength. The larger the neck size, the more the elastic strength of the sintered structure. In addition, Fig. 20 displays stress–strain curves for various initial models. The tensile performance of the NS1–NS1 model was superior to the NS1–NF1 model. As the size of sintered particles increased, the shear strength of the NS2–NF2 model decreased compared with the NS1–NF1 model. The variation in tensile stress for the nonequal radius NS–NS model confirmed the greater influence of dislocation activity on the stress generated by smaller particles.

3.4. *Effects of sintering performance on the mechanical properties*

To bridge the sintering performance to the mechanical response, Fig. 21 plots the shear modulus and shear strength as a function of sintering performance, x/W. The mechanical behavior of the sintered model was highly consistent with the aforementioned sintering results. The fitting of shear modulus and shear strength revealed that both increased linearly with the increase in the x/W ratio. A larger x/W leads to a stronger shear performance.

Fig. 22 plots the elastic modulus and tensile strength as a function of sintering performance, x/W. The fitting results in Fig. 22 indicate that the elastic modulus and tensile strength also show a linear increase trend with x/W. With the x/W becoming larger, the tensile performance became better.

The effect of the addition of NF on the interconnection of Cu NPs was more significant than that of the temperature. The results show that larger x/W, that is, larger neck size, indicates improved model sintering quality. Under the same size, the NS–NF model has better mechanical properties than the NS–NS model. The model in which NF was added to sintering at 500 K had a shear strength of 3.51 GPa, which was greater than that of the NS–NS model at the same sintering temperature. The mechanical properties of the nano-Cu sintered structure were improved by increasing the sintering temperature. However, the effect of the temperature change was less significant than that caused by the change in the sintering structure of NF particles. Structures with larger x/W have superior shear modulus, shear strength, elastic modulus, and tensile strength.

4. Conclusions

This study proposed an EAM-based MD simulation study to investigate the sintering behavior and mechanism of Cu NPs. Considering the geometric structure of sintered materials, five hybrid models comprising equal/nonequal NS–NF and NS–NS pair were established and subsequently simulated at multiple sintering temperatures. The evolution of x/W and MSD was recorded to evaluate the sintering process. Furthermore, the dislocation activity was used to analyze the atomic migration behavior during sintering. Eventually, shear simulations and tensile simulations were conducted on the sintered structure at multiple temperatures. The results revealed that (1) the influence of hybrid composition on the growth of the neck region was more significant than that of the sintering temperature. Increasing the diameter ratio can promote the atomic diffusion of particles and growth of the sintering neck. Compared with the equal dimension NS–NS model, the NS–NS models with diameter ratios of 1:2 and 1:3 had larger x/W; (2) the NS–NF model resulted in a larger x/W and MSD, which indicated superior sintering performance. The NF deformed toward the neck region, and the increased contact area improved the growth of the neck region. The stress release generated by the deformation also promoted the sintering of the Cu NPs. In the subsequent stage of sintering, the deformation degree of NF particles decreased and turned to tilt to NS particles. (3) The mechanical properties were reduced at a high shear temperature. Similarly, the mechanical properties decreased at high tensile temperatures and slower tensile rates. (4) However, the shear modulus, shear strength, elastic modulus, and tensile strength of the sintered structure were enhanced by a larger x/W ratio. The addition of NF promoted the growth of the sintered neck and increased the x/W of the sintered structure, which resulted in Cu NPs coalescing, which improved their mechanical properties. Compared with the NS1–NS1 model, the shear modulus of the NS1–NF1 model was increased by 41 %, approaching 45 GPa, and the shear strength increased by 14 %, reaching 3.51 GPa. The elastic modulus of the NS1–NF1 model increased by 49 %, reaching approximately 55.6 GPa. In addition, the tensile strength increased by 27.4 % to

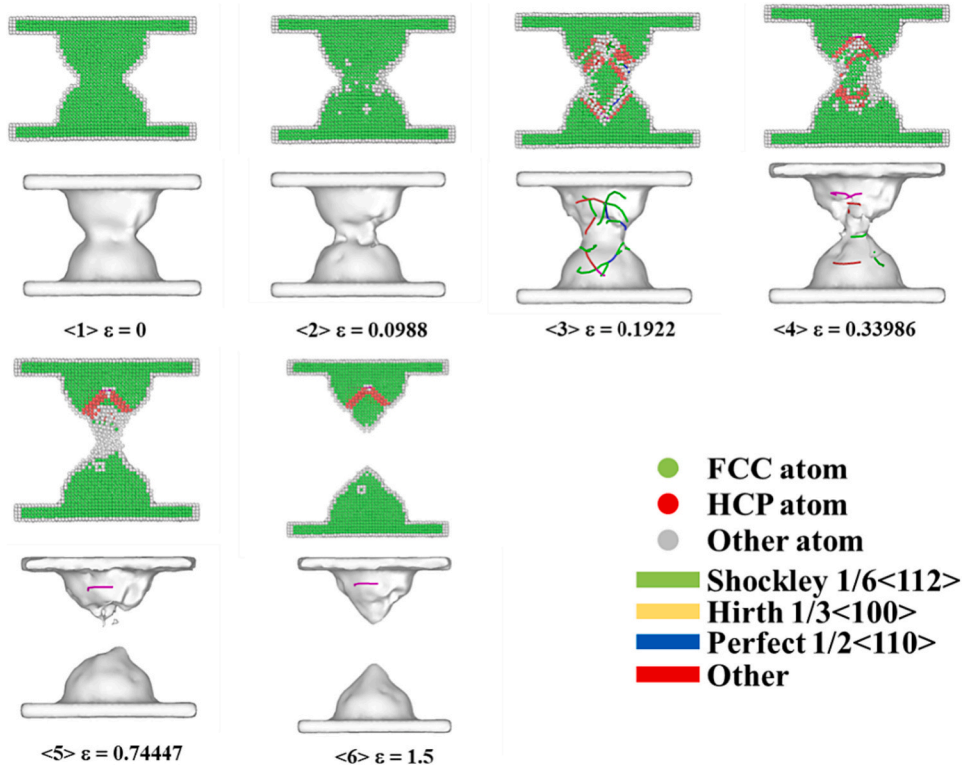

Fig. 16. Snapshots of the NS1–NS2 model during sintering: Lattice structures, HCP lattice structure, and dislocations.

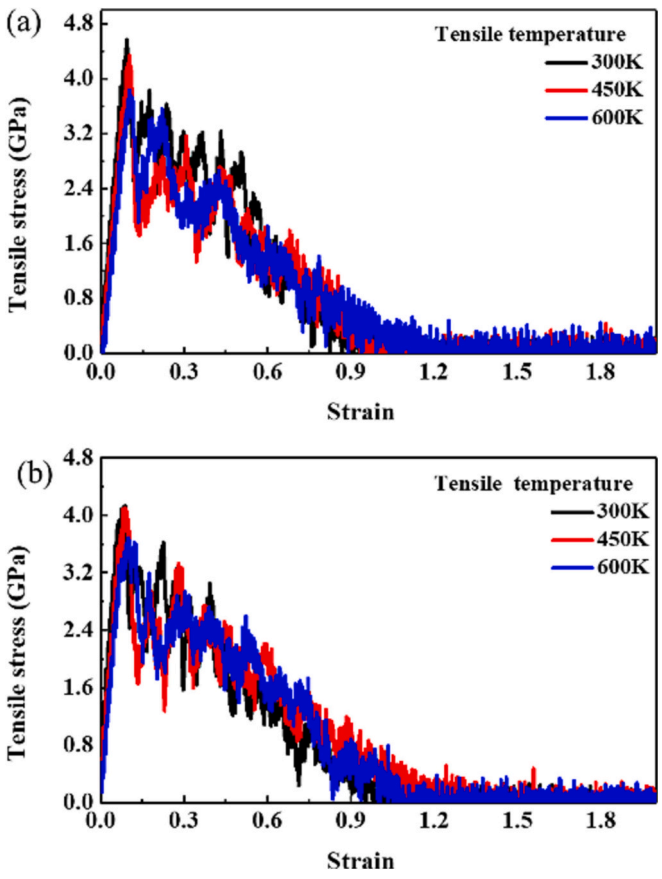

Fig. 17. (a) Tensile stress in NS1–NS1 at various tensile temperatures; (b) Tensile stress in NS1–NF1 at various tensile temperatures.

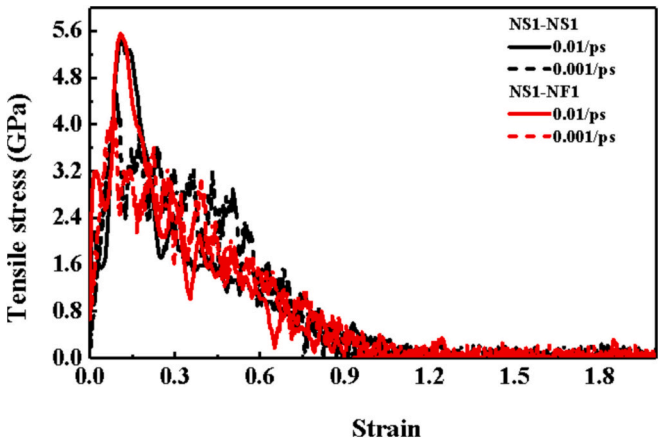

Fig. 18. Tensile simulation of tensile stress at various strain rates.

reach 4.88 GPa. This result was consistent with experimental results demonstrating that less porous nano-Cu sintered structures exhibited superior mechanical properties. This study provided theoretical research support for the application of nano-Cu sintered materials in SiC power module packaging.

CRediT authorship contribution statement

Runding Luo: Writing—original draft preparation; data collection and analysis.

Dong Hu: Technical supports on simulation; writing—review and editing.

Cheng Qian: Experiments; writing—review and editing.

Xu Liu: Simulation and analysis.

Xuejun Fan: Supervision.

Guoqi Zhang: Supervision.

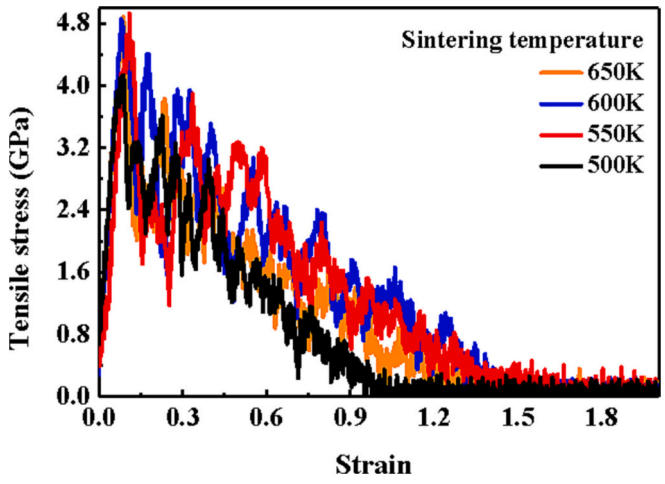

Fig. 19. NS1–NF1 tensile simulation of tensile stress at various sintering temperatures.

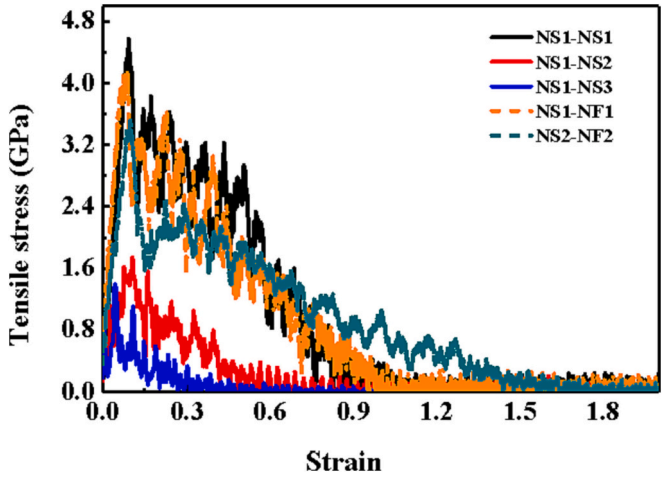

Fig. 20. Tensile stress of different sintered structures at a sintering temperature of 500 K.

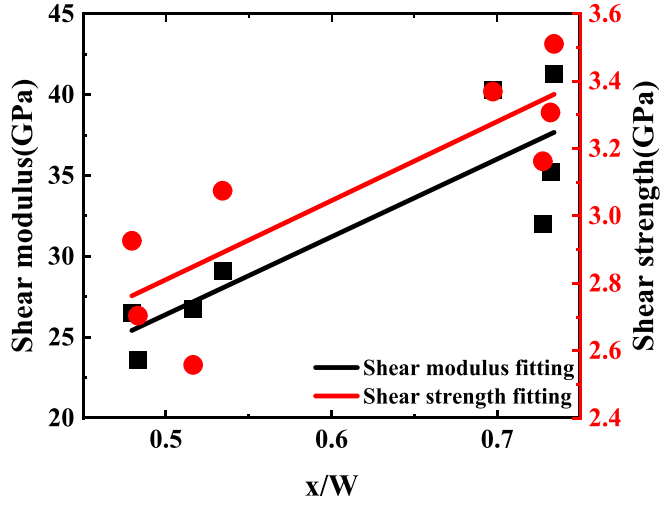

Fig. 21. Shear modulus and shear strength of the sintered structure with various x/W values.

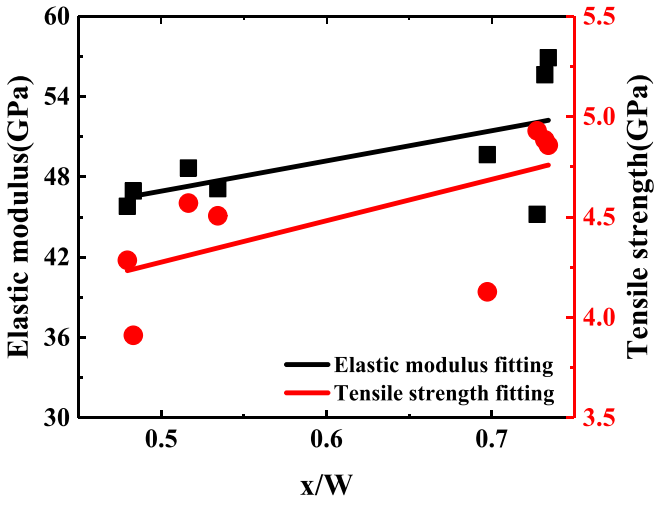

Fig. 22. Elastic modulus and tensile strength of the sintered structure with various x/W values.

Jiajie Fan: Conceptualization; methodology; writing—review and editing; project administration; funding acquisition; supervision.

Declaration of competing interest

All authors declare no conflict of interest.

Data availability

Data will be made available on request.

Acknowledgments

This work was partially supported by the National Natural Science Foundation of China (52275559), Shanghai Pujiang Program (2021PJD002), Taiyuan Science and Technology Development Funds (Jie Bang Gua Shuai Program), and Shanghai Science and Technology Development Funds (19DZ2253400).

References

[1] F. Roccaforte, et al., Emerging trends in wide band gap semiconductors (SiC and GaN) technology for power devices, Microelectron. Eng. 187 (2018) 66–77.
[2] R. Khazaka, L. Mendizabal, D. Henry, R. Hanna, Survey of high-temperature reliability of power electronics packaging components, IEEE Trans. Power Electron. 30 (5) (2014) 2456–2464.
[3] H. Yan, P. Liang, Y. Mei, Z. Feng, Brief review of silver sinter-bonding processing for packaging high-temperature power devices, Chin. J. Electr. Eng. 6 (3) (2020) 25–34.
[4] Z. Wu, J. Cai, Q. Wang, J. Wang, Low temperature Cu-Cu bonding using copper nanoparticles fabricated by high pressure PVD, AIP Adv. 7 (3) (2017), 035306.
[5] H. Ji, J. Zhou, M. Liang, H. Lu, M. Li, Ultra-low temperature sintering of Cu@ Ag core-shell nanoparticle paste by ultrasonic in air for high-temperature power device packaging, Ultrason. Sonochem. 41 (2018) 375–381.
[6] X. Liu, et al., Microstructural evolution, fracture behavior and bonding mechanisms study of copper sintering on bare DBC substrate for SiC power electronics packaging, J. Mater. Res. Technol. 19 (2022) 1407–1421.
[7] J. Nandy, S. Sahoo, H. Sarangi, Study on shape dependency of Al-alloy nanoparticles during coalescence in direct metal laser sintering: a molecular dynamics approach, Mater. Today: Proc. 41 (2021) 347–351.
[8] J. Yeom, et al., Ag particles for sinter bonding: flakes or spheres? Appl. Phys. Lett. 114 (25) (2019), 253103.
[9] C. Wang, G. Li, D. Zhang, P. Zhu, Synthesis of triangular silver nanoflakes and its application in die-attachment materials, in: 2020 21st International Conference on Electronic Packaging Technology (ICEPT), IEEE, 2020, pp. 1–4.
[10] S. Soichi, K. Suganuma, Low-temperature and low-pressure die bonding using thin Ag-flake and Ag-particle pastes for power devices, IEEE Trans. Compon. Packag. Manuf. Technol. 3 (6) (2013) 923–929.
[11] H. Zhang, S. Nagao, S. Park, S. Koga, T. Sugahara, K. Suganuma, Nano-SiC added Ag paste sintering die-attach for SiC power devices, in: Proceedings of the 5th

Electronics System-integration Technology Conference (ESTC), IEEE, 2014, pp. 1–4.
[12] C. Wang, et al., Low temperature sintered silver nanoflake paste for power device packaging and its anisotropic sintering mechanism, ACS Appl. Electron. Mater. 3 (12) (2021) 5365–5373.
[13] S. Li, et al., Sintering mechanism of Ag nanoparticle-nanoflake: a molecular dynamics simulation, J. Mater. Res. Technol. 16 (2022) 640–655.
[14] B. Cheng, A.H. Ngan, The sintering and densification behaviour of many copper nanoparticles: a molecular dynamics study, Comput. Mater. Sci. 74 (2013) 1–11.
[15] D. Hu, Z. Cui, J. Fan, X. Fan, G. Zhang, Thermal kinetic and mechanical behaviors of pressure-assisted Cu nanoparticles sintering: a molecular dynamics study, Results Phys. 19 (2020), 103486.
[16] J. Adams, S. Foiles, W. Wolfer, Self-diffusion and impurity diffusion of fee metals using the five-frequency model and the embedded atom method, J. Mater. Res. 4 (1) (1989) 102–112.
[17] L. Wang, et al., New twinning route in face-centered cubic nanocrystalline metals, Nat. Commun. 8 (1) (2017) 2142.
[18] P. Grammatikopoulos, Atomistic modeling of the nucleation and growth of pure and hybrid nanoparticles by cluster beam deposition, Curr. Opin. Chem. Eng. 23 (2019) 164–173.
[19] S. Plimpton, Fast parallel algorithms for short-range molecular dynamics, J. Comput. Phys. 117 (1) (1995) 1–19.
[20] A. Stukowski, Visualization and analysis of atomistic simulation data with OVITO–the open visualization tool, Model. Simul. Mater. Sci. Eng. 18 (1) (2009), 015012.